Map of Crystal-Field Effects in Correlated Layered t_{2g}^n Perovskites

Neda Samani,[1] Guoren Zhang[1,2,3] and Eva Pavarini[1,4]

[1]*Institute for Advanced Simulation, Forschungszentrum Jülich, 52425 Jülich, Germany*
[2]*School of Physics and Technology, Nantong University, Nantong 226019, People's Republic of China*
[3]*Key Laboratory of Materials Physics, Institute of Solid State Physics, HFIPS, Chinese Academy of Sciences, Hefei 230031, People's Republic of China*
[4]*JARA High-Performance Computing, Forschungszentrum Jülich, Germany*

Correlated metallic layered t_{2g}^n perovskites are intensively studied and yet their low-energy electronic properties remain hotly debated. Important elements of the puzzle, beside the on-site Coulomb repulsion, are the tetragonal crystal-field splitting and the spin-orbit interaction. Here, we show that they control the electronic properties principally via form and occupations of natural orbitals. We discuss consequences for shape and topology of the Fermi surface, effective masses, and metal-insulator transition, building a map of crystal-field effects. The emerging picture captures electronic-structure trends in this family of systems within a single framework.

Introduction.—Since the discovery of anomalous superconductivity in Sr_2RuO_4 [1], correlated metallic layered t_{2g}^n perovskites are at the center of very active research [2–34]. This led to the identification of novel phenomena, such as Hund's metal behavior, Van Hove singularity (VHs) effects, a topological Lifshitz transition [14–27]. Experimental and theoretical investigations were further fostered by the identification of similarities between the small-gap insulator Sr_2IrO_4 [35–37] and La_2CuO_4, in the hope of finding high-temperature superconductivity in families of systems other than the cuprates. Parallel efforts go into designing new materials with electronic properties controlled via strain [24–26], choice of substrate [29,37], or external parameters [38], as well as into identifying nontrivial topological phases. In this panorama, a key piece of understanding is incomplete: the role of the crystal-field (CF) splitting, ε_{CF}, in determining Fermi-liquid (FL) properties, its interplay with the logarithmic VHs, the band width W, and the spin-orbit (SO) coupling, λ. In short, a map of CF effects for this class of systems is missing. This is crucial not only at the fundamental level but also for applications. Indeed, the CF splitting can be tuned via (external or chemical) pressure, strain, or layering. Providing such a map is thus the aim of this Letter.

In layered t_{2g}^n perovskites the t_{2g} orbitals split into $(xz, yz) \oplus (xy)$, with $\varepsilon_{CF} = \varepsilon_{xz/yz} - \varepsilon_{xy}$. Concurrently, the xz/yz bands are one- and the xy band is two-dimensional-like; the associated bandwidths are thus one about half the size of the other, $W_{xz/yz} \sim W_{xy}/2$, and there is a VHs close to the xy-band center. A map of CF effects should show how ε_{CF} controls correlation effects in such a complex panorama. The primary indicators are spectral functions (Fig. 1) and FL low-energy ($\omega \sim 0$) properties

(Figs. 2–4), in particular the quasiparticle effective masses, $m \to m^*$, and the effective CF splitting, $\varepsilon_{CF} \to \varepsilon_{CF}^*$. In this Letter we show that the bare CF splitting, ε_{CF}, controls these properties mostly via the form of natural orbitals, $\{|\alpha\rangle\}$, and their occupations, $\{n_\alpha\}$. This provides the key to disentangle the results; the emerging picture yields a unifying framework capturing electronic-structure trends.

The first consequence is that, for $\lambda = 0$, each effective mass m_α^* is in practice determined by its n_α [39]. Thus, $m_{xz/yz}^*$ reaches the largest value around $n_{xz/yz} \sim 1$. The quasi-two-dimensional xy band differs in that it exhibits a VHs at $n_{xy} = n_{xy}^{VH} > 1$, which, in turn, can influence the value of m_{xy}^* [16–20]. Here, we find that the VHs is less crucial than believed. It attracts the maximum of m_{xy}^* toward n_{xy}^{VH}, but it loses importance with approaching the metal-insulator transition (MIT). Next, at the Fermi surface, under circumstances, we find a CF splitting reduction ($|\varepsilon_{CF}^*| < |\varepsilon_{CF}|$), instead of the more conventional [40–43] enhancement ($|\varepsilon_{CF}^*| > |\varepsilon_{CF}|$). In addition, metallic orbital ordering (OO) is only obtained for $|\varepsilon_{CF}| \sim W_{xz/yz}-$differently than in the Mott regime [10,34,40–43]. Even then, contrarily to what often assumed, filled and empty bands are only inert for extreme $|\varepsilon_{CF}|$. Finally, switching on the SO interaction mostly affects FL properties via changes in $\{|\alpha\rangle, n_\alpha\}$ and the topological point.

Model and method.—We adopt the local-density approximation + dynamical mean-field theory (LDA + DMFT) approach [44–47]; the Wannier basis is obtained using projectors on top of linearized augmented plane-wave band-structure calculations [48]. The model solved is the t_{2g} Hubbard Hamiltonian
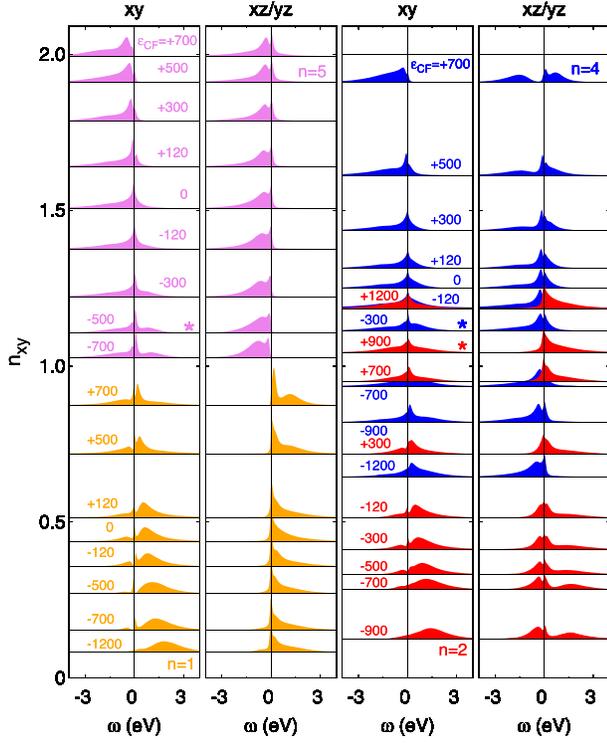
FIG. 1. Orbital-resolved spectral functions, $A_{m,m}(\omega)$, for increasing crystal-field splitting, ε_{CF} (meV). Each curve is shifted vertically by an amount proportional to n_{xy}. Temperature: 290 K. For each filling, n, the ε_{CF} yielding the largest xy effective mass, $m_{xy}^\star$, is labeled with a $\star$.

$$H = -\sum_{ii'\sigma\sigma'}\sum_{m,m'} t_{m\sigma,m'\sigma'}^{i,i'} c_{im\sigma}^\dagger c_{i'm'\sigma'} + U\sum_{im}\hat{n}_{im\uparrow}\hat{n}_{im\downarrow}$$

$$+\frac{1}{2}\sum_i\sum_{\substack{\sigma m\neq\sigma'm'}}(U-2J-J\delta_{\sigma,\sigma'})\hat{n}_{im\sigma}\hat{n}_{im'\sigma'}$$

$$-J\sum_i\sum_{m\neq m'}(c_{im\uparrow}^\dagger c_{im\downarrow}^\dagger c_{im'\uparrow}c_{im'\downarrow} + c_{im\uparrow}^\dagger c_{im\downarrow}c_{im'\downarrow}^\dagger c_{im'\uparrow}),$$

$$(1)$$

where $m = xz, xy, yz$ and $\hat{n}_{im\sigma} = c_{im\sigma}^\dagger c_{im\sigma}$. The on-site ($i' = i$) energy matrix, with elements $\varepsilon_{m\sigma,m'\sigma'} = -t_{m\sigma,m'\sigma'}^{i,i}$, yields the CF splitting (ε_{CF}) and the SO coupling (λ) [49]. In order to single out the effects of ε_{CF}, unless differently specified, we keep other parameters fixed. For the screened Coulomb interactions, we thus set $(U, J) = (2.3, 0.4)$ eV, established values for ruthenates, rhodates, and iridates; similarly, we adopt hopping integrals, $t_{m\sigma,m'\sigma'}^{i,i'}$ with $i \neq i'$, and the SO interaction, λ, calculated for Sr_2RuO_4 [11]. Thus, the band widths are $W_{xz/yz} \sim W_{xy}/2 \sim 1.5$ eV, and $\lambda \sim 100$ meV. The site symmetry is D_{4h}, so that, if $\lambda = 0$, the t_{2g} natural orbitals decompose into $b_{2g} \oplus e_g$, with $b_{2g} = xy$ and $e_g = (xz, yz)$. We study the regime $-3J < \varepsilon_{CF} < 3J$, which reaches the limit in which
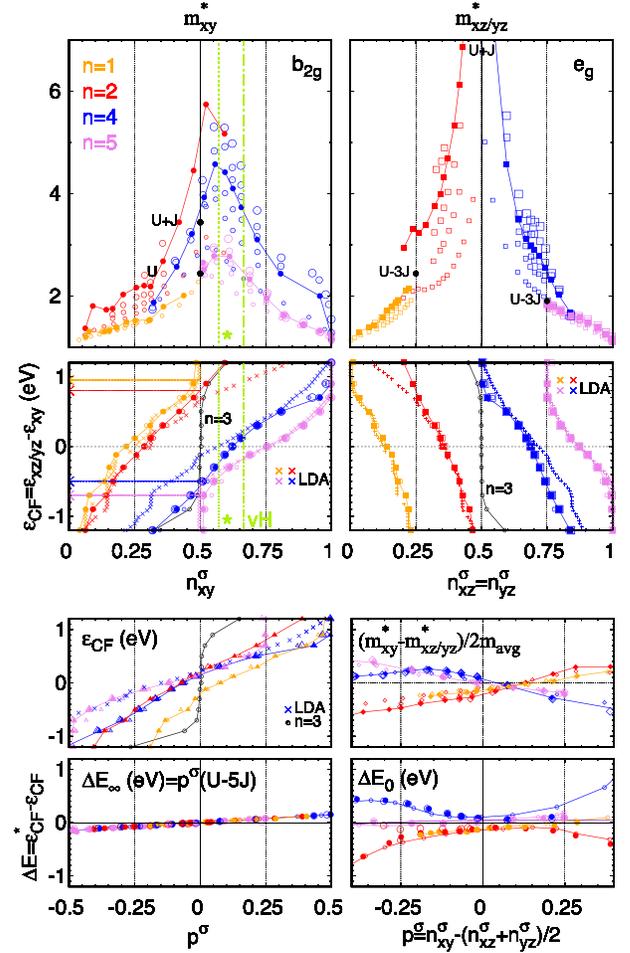
FIG. 2. Top panels: effective masses, m_α^* (first row), and bare CF splitting, ε_{CF} (second row), as a function of natural occupations per spin, $n_\alpha^\sigma = n_\alpha/2$. Symbols of increasing size: temperature decreasing from 1150 to 145 K; at 290 K (filled symbols) all key features are captured. Filled black circles: reduced-size models results and associated atomic gap. Arrows: ε_{CF} yielding $n_{xy}^\sigma = 0.5$. Bottom panels: various quantities versus orbital polarization p^σ. First row: ε_{CF} and relative mass anisotropy, with $m_{avg} = (m_{xy}^* + m_{xz}^* + m_{yz}^*)/3$. Second row: $\Delta E = \varepsilon_{CF}^* - \varepsilon_{CF}$, effective CF shift; infinite (ΔE_∞) and low (ΔE_0) Matsubara-frequency limit.

spin-state transitions are possible. We use the weak-coupling continuous-time quantum Monte Carlo quantum-impurity solver [51], in the implementation of Refs. [10,11]. The orbital polarization [50,52,53] is given by $p^\sigma = n_{xy}^\sigma - (n_{xz}^\sigma + n_{yz}^\sigma)/2$. We define $n_m^\sigma = \langle\hat{n}_{im\sigma}\rangle$, $n_m = \sum_\sigma n_m^\sigma$, and $n = \sum_m n_m$.

Crystal-field map.—Our results show that ε_{CF} changes electronic properties mostly via the form and occupations of natural orbitals (Figs. 1 and 2). Inverting the relations $\{n_\alpha(\varepsilon_{CF})\}$ thus provides the key to unify the data. In fact, for distinct fillings n, different values of ε_{CF} can lead to similar behavior. This is, e.g., shown in Fig. 2, top panels, second row (arrows) for $n_{xy}^\sigma = 0.5$. In the rest of the Letter,
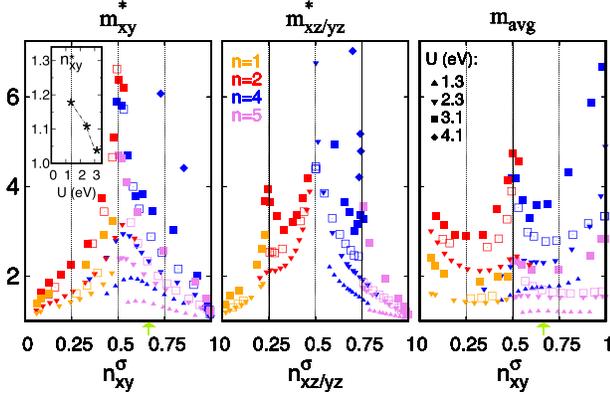
FIG. 3. Evolution of effective masses with increasing U at fixed temperature. Filled symbols: $J = 0.4$ eV. Empty symbols: $J = 0.7$ eV. Calculations at $\beta = 10$ eV^{-1} are sufficient to capture the trends. Green arrow: n_{xy}^{VH}. Inset: $n_{xy}^\star$ value ($n = 4$), yielding the maximum of m_{xy}^* for increasing U.

we discuss all results based on this and the associated emerging unifying framework.

Metal-insulator transition and orbital ordering.—The first key question is how large $|\varepsilon_{\mathrm{CF}}|$ should be, everything else staying the same, for the realistic Coulomb integrals $(U, J) \sim (2.3, 0.4)$ eV to either (i) trigger an orbitally ordered MIT or (ii) stabilize metallic OO. This point is addressed in Fig. 1. We find that the system basically stays metallic for all n. With increasing $\varepsilon_{\mathrm{CF}}$ there is a smooth $e_g \to b_{2g}$ transfer of spectral weight; the process is slower for even n. Eventually, a metallic ferro-OO state is realized, but only in the (unrealistic) limit $|\varepsilon_{\mathrm{CF}}| \sim W_{xz/yz} \sim 3J$. Furthermore, in this regime, the orbital polarization p^σ, the order parameter for OO, is weakly temperature-dependent (Fig. 2). This behavior differs qualitatively from that of Kugel-Khomksii [52] insulators, which exhibit a second-order OO phase transition [40,52]. In fact, in order to reach the MIT, U has to sizably increase (Fig. 3).

Effective masses.—Figure 2 shows that the effective masses $\{m_\alpha^*\}$ are essentially determined by form and occupations of the natural orbitals, with $\{m_\alpha^*\} = \{m_\alpha^*(n_\alpha)\}$. However, while $m_{xz/yz}^*$ diverges at half filling [54], m_{xy}^* stays finite and has a maximum at $n_{xy}^\star \sim 1 + \delta n_{xy}^\star$, with $\delta n_{xy}^\star \sim 0.1$. This shift $\delta n_{xy}^\star$ can be traced down to the logarithmic VHs in the noninteracting xy spectrum, located at $n_{xy}^{\mathrm{VH}} \sim 1.3 > n_{xy}^\star$. An important question [16–20] is how the latter affects the MIT and the mass hierarchy. To clarify these points, in Fig. 3 we show $\{m_\alpha^*\}$ for increasing U. The figure shows (inset) that the maximum of m_{xy}^* moves toward half filling ($n_{xy} = 1$) as U increases: the exact position of the VHs, controlled by long-range hopping integrals, loses relevance approaching the MIT. Conversely, the role of integer fillings grows. In fact, $m_{xz/yz}^*$ acquires maxima when the xz/yz bands are filled with either one or three electrons ($n_{xz/yz}^\sigma = 0.25$, 0.75). This is reflected in the average

correlation strength, measured by the average mass, $m_{\mathrm{avg}} = (m_{xy}^* + m_{xz}^* + m_{yz}^*)/3$, right panel of Fig. 3; also the latter, besides the peaks at $n_{xz/yz}^\sigma \to 0.5$, acquires maxima for $n_{xz/yz}^\sigma \to 0.25$, 0.75, while it shows a local minimum around $n_{xy}^\sigma \sim n_{xy}^{\mathrm{VH}}$. Finally, Fig. 2 shows that the relative mass anisotropy, $(m_{xy}^* - m_{xz/yz}^*)/2m_{\mathrm{avg}}$, has a fixed point at $p_0^\sigma \sim 0.08$, i.e., for $n_{xy}^\sigma = n/6 + 2p_0^\sigma/3$, and thus the mass difference changes sign at a n_{xy} value that can be far from n_{xy}^{VH}, a result that stays with increasing U (see Supplemental Material [50]).

Model-size collapse.—Here, we discuss when, for integer partial occupations, the $t_{2g}^n = e_g^m b_{2g}^{n-m}$ problem can be mapped into a reduced-size one, including only either (i) the b_{2g} ($m = 0$, 4) or (ii) the e_g ($n - m = 0$, 2) orbital degrees of freedom. We first consider case (i). From b_{2g}^1 single-band calculations we find $m_{xy}^* \sim 2.45$. Figure 2 shows that this point (filled black circle) lies at the juncture between the $n = 1$ and $n = 5$ curve for the three-band model; this limit is only reached for extreme $\varepsilon_{\mathrm{CF}}$ values, however. In fact, at exactly $n_{xy}^\sigma = 0.5$, the xy spectral functions for the one- and three-band models are very similar, but deviations appear very quickly moving away from $n_{xy}^\sigma = 0.5$. A similar conclusion applies to case (ii) for both the $e_g^1 b_{2g}^0$ ($n = 1$) and $e_g^3 b_{2g}^2$ ($n = 5$) configurations, as might be seen in Fig. 2. Thus, eventually, a model-size collapse does occur, but only for extreme $|\varepsilon_{\mathrm{CF}}|$. These conclusions extend to the $e_g^2 b_{2g}^2$ and $e_g^2 b_{2g}^0$ cases [50]. Remarkably, at first glance, in the Mott phase, a size collapse is easier. This is because, with increasing U, the n_α are progressively squeezed toward integer values (Fig. 3), compatible with a reduced-size model limit. However, unless $|\varepsilon_{\mathrm{CF}}|$ is extreme, three-band effects persist, as shown, e.g., from the fact that the gap is smaller than in the corresponding reduced-size model [50,56].

Fermi surface.—The shape of the Fermi surface is modified by low-energy ($\omega \sim 0$) many-body effects transforming $\varepsilon_{\mathrm{CF}}$ into the effective CF splitting $\varepsilon_{\mathrm{CF}}^*$ [11,50]. Figure 2 (bottom) shows ΔE_0, the difference $\varepsilon_{\mathrm{CF}}^* - \varepsilon_{\mathrm{CF}}$, calculated at the lowest Matsubara frequency. Overall, ΔE_0, is larger and more strongly p^σ-dependent for even than for odd n. Most importantly, there is a large $\varepsilon_{\mathrm{CF}}$ interval in which $\Delta E_0/\varepsilon_{\mathrm{CF}} < 0$, so that $\varepsilon_{\mathrm{CF}}$ is effectively *reduced* [57]. We find that this unusual behavior reflects the underlying Fermi liquid. At $T = 0$, in a Fermi liquid, ΔE_0 is determined by the natural occupations via the Luttinger theorem; since here the $\{n_\alpha\}$ are weakly T-dependent, ΔE_0 can thus be estimated from the inverse function $\varepsilon_{\mathrm{CF}}(p_{\mathrm{LDA}}^\sigma)$, where p_{LDA}^σ is the LDA polarization: $\Delta E_0 \sim \varepsilon_{\mathrm{CF}}(p^\sigma) - \varepsilon_{\mathrm{CF}}(p_{\mathrm{LDA}}^\sigma)$. This yields a picture in line with DMFT results, as may be seen for, e.g., the $n = 4$ case in Fig. 2, third row, left [$\varepsilon_{\mathrm{CF}}(p_{\mathrm{LDA}}^\sigma)$, blue crosses].

Spin-orbit interaction.—For Sr_2RuO_4, SO effects have been found to only moderately affect $\{m_\alpha^*\}$ in the
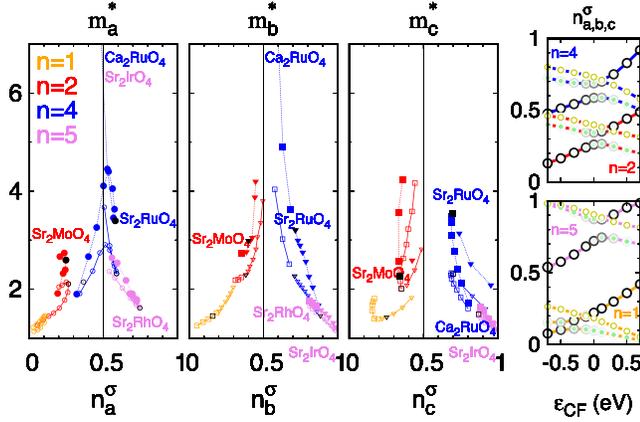
FIG. 4. Left: effective masses in natural orbital basis $|a\rangle_\sigma = a_1|xy\rangle_{-\sigma} + a_2|xz + 2i\sigma yz\rangle_\sigma$, $|b\rangle_\sigma = |xz - 2i\sigma yz\rangle_\sigma$, and $|c\rangle_\sigma = \overline{a_2}|xy\rangle_{-\sigma} - \overline{a_1}|xz + 2i\sigma yz\rangle_\sigma$. Circles: $|a\rangle_\sigma$. For $|b\rangle_\sigma$ and $|c\rangle_\sigma$: squares, $n_b > n_c$; triangles, $n_b < n_c$. Black symbols: $\varepsilon_{CF} \sim 120$ meV. Other symbols as in Fig. 2. Right: n_a^σ, n_b^σ, and n_c^σ as a function of ε_{CF}, with projections (circles) on $|xy\rangle_\sigma$ (black), $|b\rangle_\sigma$, (yellow), and $|xz + 2i\sigma yz\rangle_\sigma$ (green).

$\alpha = xy, xz, yz$ basis [19,20,58]. Under conditions, this conclusion can be generalized. Indeed, for all ε_{CF} and n, switching on a *moderate* SO coupling ($\lambda \sim 100$ meV) leads to small differences not only in the $\{m_\alpha^*(n_\alpha)\}$ curves, but in the full spectral functions, even down to $k_B T \sim \lambda/5$ [59]. Still, a finite λ brings radical changes in the form of natural orbitals, which become the Kramers doublets $\{|\tilde{\alpha}\rangle\}$ [50]. The least occupied of these doublets is $|a\rangle_\sigma = a_1|xy\rangle_{-\sigma} + a_2|xz + 2i\sigma yz\rangle_\sigma$, with $|a_1|^2 + |a_2|^2 = 1$; it is convenient to define the remaining two as $|b\rangle_\sigma = |xz - 2i\sigma yz\rangle_\sigma$ and $|c\rangle_\sigma = \overline{a_2}|xy\rangle_{-\sigma} - \overline{a_1}|xz + 2i\sigma yz\rangle_\sigma$; the order of their occupations switches at a topological point [60]. The change in natural orbitals, in turn, influences the electronic properties. Figure 4 shows that, for $|b\rangle_\sigma$, decoupled by symmetry, $m_b^* = m_b^*(n_b)$, as before. The topological point (right panel), however, results in the folding of m_a^* and m_c^*, which can form closed loops connecting (via a three-band phase) reduced-size-model phases of different nature and size, e.g., for $n = 5$, a b_{2g}^1 and an e_g^3 state [50]. Remarkably, except for extreme ε_{CF}, the interorbital elements of the effective mass tensor remain relatively small. Thus, the formation of Kramers states can enhance, in comparison, the masses of either the least or the most occupied channel(s), but a metallic system stays metallic [61]. The picture substantially changes with increasing U and λ, however: the interorbital masses increase, becoming eventually comparable with intraorbital ones [50], and finally supporting a SO-assisted Mott state.

Materials and conclusions.—The results obtained provide a unifying framework in which electronic trends in layered t_{2g}^n perovskites can be understood. FL properties are mostly controlled by form and occupations of natural orbitals. Thus, in the absence of SO interaction,

$m_\alpha^* = m_\alpha^*(n_\alpha)$, and the largest masses are found at $n_{xz/yz} \sim 1$ (e_g channel) and $n_{xy} \sim 1 + \delta n_{xy}^\star$ (b_{2g} channel); Fig. 2. The maximum of m_{xy}^* moves progressively away from n_{xy}^{VH} and toward $n_{xy} = 1$ with increasing the Coulomb repulsion, so that the position of the VHs loses importance approaching the MIT; Fig. 3. The relative mass anisotropy ($m_{xy}^* - m_{xz/yz}^*$)/$2m_{avg}$ has a fixed point at p_0^σ and can change sign for a n_{xy} value that can be far from n_{xy}^{VH}; Fig. 2. Overall, CF effects are stronger and masses larger for even than for odd n. Switching on λ changes the natural orbitals $\{|\alpha\rangle\}$ into Kramers doublets; while for the symmetry-decoupled $|b\rangle_\sigma$ doublet stays true that $m_b^* = m_b^*(n_b)$, in the remaining two channels the masses fold around the topological point; Fig. 4. The paradigmatic system Sr_2RuO_4 is close to such a point ($\lambda \sim \varepsilon_{CF} \sim 120$ meV, $n = 4$), and it is metallic with $m_{xy}^* > m_{xz/yz}^*$. The isoelectronic Ca_2RuO_4, for which W is reduced by octahedral distortion and rotations, and which has a relatively larger $\varepsilon_{CF} > 0$, is an xy-OO insulator; here, the large xz/yz component of $|a\rangle_\sigma$ helps in making m_a^* diverge [10,55], while m_{xy}^* is relatively small for the almost filled xy orbital; see Fig. 4. In the $n = 2$ case a small CF splitting can yield $m_{xy}^* < m_{xz/yz}^*$, as reported for Sr_2MoO_4 [21], but, e.g., uniaxial pressure could invert the order. For odd $n = 1, 5$, the masses always remain relatively small in comparison, everything else staying the same. Indeed Sr_2RhO_4, similar to Sr_2RuO_4 but with an electron more ($n = 5$), is less correlated. Furthermore, for odd n, correlation deforms the Fermi surface mostly via the many-body renormalization of the SO coupling, $\lambda \to \lambda^*$, while the CF renormalization, $\varepsilon_{CF} \to \varepsilon_{CF}^*$, plays a smaller role, an example being again Sr_2RhO_4 [12]. In the case Sr_2IrO_4 ($n = 5$), with structure similar to Sr_2RhO_4 but a larger $\lambda \sim 350$ meV and $\varepsilon_{CF} \sim 0.3$ eV, a small gap opens. This can be understood in two steps. Switching on a moderate λ for $\varepsilon_{CF} \sim 0.3$ eV pushes n_a^σ closer to 0.5 and $n_{b/c}^\sigma$ closer to 1 (Fig. 4, right panel) and eventually m_a^* reaches a maximum, $m_a^* \sim 1 + 3(m_{avg} - 1)$. Further increasing λ suppresses spin-orbital degeneracy, enhancing off-diagonal masses (see Supplemental Material [50]); the evolution is slow, but, if U/W is sufficiently large, a partial effect can open a small gap. Finally, for the whole class of systems studied, unless ε_{CF} is extreme, a full model-size collapse is not obtained.

Increasing correlation strength, for most ε_{CF} values, pushes the system toward integer natural occupations. Typically $3d$ compounds have a larger U/W ratio in comparison, and an insulator can be obtained more easily, even for odd n. An example is the small-gap system Sr_2VO_4 ($n = 1$), with $\varepsilon_{CF} < 0$, undergoing an insulator-to-metal transition under pressure [62,63]. For $n = 2$, a representative case Sr_2CrO_4 [64–66], with $\varepsilon_{CF} \sim 150$ meV, remaining insulating under pressure [63]. Sr_2MnO_4 and Sr_2TcO_4 are also insulators; indeed, for $n = 3$, everything else staying the same, all masses are very high in

comparison to other fillings, since the electronic configuration remains close to $e_g^2 b_{2g}^1$ except for extreme ε_{CF}; Fig. 2.

In conclusion, this Letter provides a map of CF effects on electronic properties of correlated layered t_{2g}^n perovskites, which shows the crucial role played by form and occupations of natural orbitals, and ties together known families of systems in a unifying framework, providing guidelines to tune properties via external parameters such as strain and pressure or by layering.

[1] Y. Maeno, H. Hashimoto, K. Yoshida, S. Nishizaki, T. Fujita, J. G. Bednorz, and F. Lichtenberg, Nature (London) **372**, 532 (1994).

[2] A. P. Mackenzie, J. Supercond. Novel Magn. **33**, 177 (2020).

[3] K. Kinjo et al., Science **376**, 6591 (2022).

[4] E. M. Pärschke, K. Wohlfeld, K. Foyevtsova, and J. van den Brink, Nat. Commun. **8**, 686 (2017).

[5] S. Ghosh, A. Shekhter, F. Jerzembeck, N. Kikugawa, D. A. Sokolov, M. Brando, A. P. Mackenzie, C. W. Hicks, and B. J. Ramshaw, Nat. Phys. **17**, 199 (2021).

[6] H. Suzuki et al., Nat. Mater. **18**, 563 (2019).

[7] A. Horvat, R. Žitko, and J. Mravlje, Phys. Rev. B **96**, 085122 (2017).

[8] B. Zwartsenberg et al., Nat. Phys. **16**, 290 (2020).

[9] B. Zwartsenberg et al., Phys. Rev. B **105**, 245130 (2022).

[10] E. Gorelov, M. Karolak, T. O. Wehling, F. Lechermann, A. I. Lichtenstein, and E. Pavarini, Phys. Rev. Lett. **104**, 226401 (2010).

[11] G. Zhang, E. Gorelov, E. Sarvestani, and E. Pavarini, Phys. Rev. Lett. **116**, 106402 (2016).

[12] G. Zhang and E. Pavarini, Phys. Rev. B **99**, 125102 (2019).

[13] H. J. Lee, C. H. Kim, and A. Go, Phys. Rev. B **102**, 195115 (2020).

[14] F. Jerzembeck, H. S. Røising, A. Steppke, H. Rosner, D. A. Sokolov, N. Kikugawa, T. Scaffidi, S. H. Simon, A. P. Mackenzie, and C. W. Hicks, Nat. Commun. **13**, 4596 (2022).

[15] Z. P. Yin, K. Haule, and G. Kotliar, Nat. Mat. **10**, 932 (2011).

[16] L. de' Medici, J. Mravlje, and A. Georges, Phys. Rev. Lett. **107**, 256401 (2011).

[17] J. Mravlje, M. Aichhorn, T. Miyake, K. Haule, G. Kotliar, and A. Georges, Phys. Rev. Lett. **106**, 096401 (2011).

[18] A. Georges, L. de' Medici, and J. Mravlje, Annu. Rev. Condens. Matter Phys. **4**, 137 (2013).

[19] M. Kim, J. Mravlje, M. Ferrero, O. Parcollet, and A. Georges, Phys. Rev. Lett. **120**, 126401 (2018).

[20] N. O. Linden, M. Zingl, C. Hubig, O. Parcollet, and U. Schollwöck, Phys. Rev. B **101**, 041101(R) (2020).

[21] J. Karp, M. Bramberger, M. Grundner, U. Schollwöck, A. J. Millis, and M. Zingl, Phys. Rev. Lett. **125**, 166401 (2020).

[22] V. Sunko et al., npj Quantum Mater. **4**, 46 (2019).

[23] A. Kreisel, C. A. Marques, L. C. Rhodes, X. Kong, T. Berlijn, R. Fittipaldi, V. Granata, A. Vecchione, P. Wahl, and P. J. Hirschfeld, npj Quantum Mater. **6**, 100 (2021).

[24] M. E. Barber et al., Phys. Rev. B **100**, 245139 (2019).

[25] A. Chronister et al., npj Quantum Mater. **7**, 113 (2022).

[26] A. Pustogow et al., Nature (London) **574**, 72 (2019).

[27] F. B. Kugler, M. Zingl, H. U. R. Strand, S.-S. B. Lee, J. von Delft, and A. Georges, Phys. Rev. Lett. **124**, 016401 (2020).

[28] K. Jenni et al., Phys. Rev. B **103**, 104511 (2021).

[29] J. Wu, H. P. Nair, A. T. Bollinger, X. He, I. Robinson, N. J. Schreiber, K. M. Shen, D. G. Schlom, and I. Božović, Proc. Natl. Acad. Sci. U.S.A. **117**, 10654 (2020).

[30] E. Pavarini, Science **376**, 350 (2022).

[31] Z. Y. Song, X.-C. Jiang, and Y.-Z. Zhang, Phys. Rev. B **102**, 245124 (2020).

[32] R. Fittipaldi et al., Nat. Commun. **12**, 5792 (2021).

[33] M. Malvestuto et al., Phys. Rev. B **88**, 195143 (2013).

[34] G. Zhang and E. Pavarini, Phys. Rev. B **95**, 075145 (2017).

[35] J. Dai, E. Calleja, G. Cao, and K. McElroy, Phys. Rev. B **90**, 041102(R) (2014).

[36] S. Fujiyama, H. Ohsumi, T. Komesu, J. Matsuno, B. J. Kim, M. Takata, T. Arima, and H. Takagi, Phys. Rev. Lett. **108**, 247212 (2012).

[37] G. Cao and P. Schlottmann, Rep. Prog. Phys. **81**, 042502 (2018).

[38] D. Haskel, G. Fabbris, M. Zhernenkov, P. P. Kong, C. Q. Jin, G. Cao, and M. van Veenendaal, Phys. Rev. Lett. **109**, 027204 (2012).

[39] For temperature above coexistence regions.

[40] E. Pavarini, E. Koch, and A. I. Lichtenstein, Phys. Rev. Lett. **101**, 266405 (2008).

[41] E. Pavarini, S. Biermann, A. Poteryaev, A. I. Lichtenstein, A. Georges, and O. K. Andersen, Phys. Rev. Lett. **92**, 176403 (2004).

[42] X.-J. Zhang, E. Koch, and E. Pavarini, Phys. Rev. B **102**, 035113 (2020).

[43] X.-J. Zhang, E. Koch, and E. Pavarini, Phys. Rev. B **106**, 115110 (2022).

[44] V. Anisimov, A. I. Poteryaev, M. A. Korotin, A. O. Anokhin, and G. Kotliar, J. Phys. Condens. Matter **9**, 7359 (1997).

[45] A. I. Lichtenstein and M. I. Katsnelson, Phys. Rev. B **57**, 6884 (1998).

[46] For a pedagogical introduction, see, e.g., The LDA + DMFT approach to strongly correlated materials, *Modeling and Simulation*, edited by E. Pavarini, E. Koch, D. Vollhardt, and A. Lichtenstein (Verlag des Forschungszentrum Jülich, Jülich, 2011), Vol. 1.

[47] E. Pavarini, Riv. Nuovo Cimento **44**, 597 (2021).

[48] P. Blaha, K. Schwarz, G. K. H. Madsen, D. Kvasnicka, and J. Luitz, WIEN2k, *An Augmented Plane Wave + Local Orbitals Program for Calculating Crystal Properties* (Wien, Austria, 2001); P. Blaha, K. Schwarz, P. Sorantin, and S. Trickey, Comput. Phys. Commun. **59**, 399 (1990).

[49] The parameters ε_{CF} and λ can be, e.g., obtained as $\varepsilon_{\text{CF}} = \varepsilon_{xz\sigma,xz\sigma} - \varepsilon_{xy\sigma,xy\sigma}$ and $\lambda = |\varepsilon_{yz\uparrow,xz\uparrow} - \varepsilon_{xz\uparrow,yz\uparrow}|$ [50].

[50] See Supplemental Material at http://link.aps.org/supplemental/10.1103/PhysRevLett.132.236505 for more details.

[51] E. Gull, A. J. Millis, A. I. Lichtenstein, A. N. Rubtsov, M. Troyer, and P. Werner, Rev. Mod. Phys. **83**, 349 (2011).

[52] K. I. Kugel' and D. I. Khomskii, Zh. Eksp. Teor. Fiz. **64**, 1429 (1973) [Sov. Phys. JETP **37**, 725 (1973)].

[53] X-J. Zhang, E. Koch, and E. Pavarini, Phys. Rev. B **105**, 115104 (2022).

[54] In an early idealized-model study [55], this was suggested as possible cause of the MIT in $Ca_{2-x}Sr_xRuO_4$.

[55] A. Liebsch and H. Ishida, Phys. Rev. Lett. **98**, 216403 (2007).

[56] G. Zhang and E. Pavarini, Phys. Rev. Lett. **131**, 036504 (2023). Here similar conclusion was drawn for the SO coupling λ, in the case of doped iridates.

[57] This differs from the Hartree-Fock high-energy shift, $\Delta E_\infty = p^\sigma(U - 5J)$, which, with the exception of a tiny interval, has the same sign of ε_{CF}; see Fig. 2. Conversely, at $\omega \sim 0$ the Hund's rule coupling J tends to reduce $|\varepsilon_{CF}|$ when the latter favors a lower spin state.

[58] E. Sarvestani, G. Zhang, E. Gorelov, and E. Pavarini, Phys. Rev. B **97**, 085141 (2018).

[59] For $n = 2$ the masses are reduced.

[60] In the atomic limit, for $\varepsilon_{CF} = 0$, $|a\rangle_\sigma$ is the $j = 1/2$ doublet, while states $|b\rangle_\sigma$ and $|c\rangle_\sigma$ form the $j = 3/2$ quartet.

[61] The maximum mass obtained in this way is $m^*_{max} \sim 1 + 3\{m_{avg} - [(m^*_b + 2)/3]\}$.

[62] S. Karmakar and P. S. Malavi, Phys. Rev. Lett. **114**, 166402 (2015).

[63] T. Yamauchi, T. Shimazu, D. Nishio-Hamane, and H. Sakurai, Phys. Rev. Lett. **123**, 156601 (2019).

[64] T. Ishikawa, T. Toriyama, T. Konishi, H. Sakurai, and Y. Ohta, J. Phys. Soc. Jpn. **86**, 033701 (2017).

[65] H. Sakurai, J. Phys. Soc. Jpn. **83**, 123701 (2014).

[66] B. Pandey, Y. Zhang, N. Kaushal, R. Soni, L.-F. Lin, W.-J. Hu, G. Alvarez, and E. Dagotto, Phys. Rev. B **103**, 045115 (2021).